Manipulating the mechanical strength and thermal conductivity of a Mg-4Zn-0.6Zr alloy through Ca addition

Kaicheng Wang[a], Xingjian Zhao[b], Jie Yin[a], Fang Yi[c], Ruifeng Li[d], Dikai Guan[b], Yonghao Gao[a*]

a. School of Materials and Engineering, Central South University, Changsha 410083, China

b. Department of Mechanical Engineering, School of Engineering, University of Southampton, Southampton, SO17 1BJ, UK

c. Hunan Xiangya Stomatological Hospital, Central South University, Changsha 410000, China

d. School of Materials Science and Engineering, Jiangsu University of Science and Technology, Zhenjiang 212100, China

Abstract

In this study, the microstructure, mechanical properties, and thermal conductivity of as-extruded Mg-4Zn-0.6Zr-xCa (x = 0, 0.3, 0.6, 0.9 wt.%) alloys were investigated. The results revealed a bimodal grain size distribution in all the alloys due to incomplete dynamic recrystallization (DRX), characterized by the coexistence of elongated deformed grains and equiaxed DRX grains. The bimodal grain size distribution enhanced the mechanical properties of the studied alloys. Furthermore, Ca alloying facilitated the formation of $Ca_2Mg_6Zn_3$ phases, through which the DRX extent was also enhanced. The precipitation of secondary phases, along with the increased DRX induced by Ca addition, was beneficial in eliminating the lattice distortion of the alloys, resulting in improved thermal conductivity compared to the Ca-free Mg-4Zn-0.6Zr alloy. The optimum combination of mechanical properties and thermal conductivity was achieved in the Mg-4Zn-0.6Zr-0.6Ca alloy, with yielding strength, ultimate tensile strength, tensile fracture elongation, and thermal conductivity values of 271 MPa, 318 MPa, 17.6%, and 123.9 W/(m·K), respectively. This work demonstrates that Mg-Zn-Zr-Ca-based alloys can be developed with high strength and high thermal conductivity, significantly expanding the industrial application of magnesium alloys.

Keywords*:* Magnesium Alloys; Microstructure; Mechanical Properties; Thermal Conductivity; Secondary Phases

* Corresponding author: Yonghao Gao, Email: gaoyonghao_009@163.com

1. Introduction

The rapid advancement of electronic devices is revolutionizing our modern life at an unprecedented pace. The performance of these devices is being significantly and rapidly improved at the cost of ever-increasing energy consumption. Unfortunately, a considerable fraction of the energy consumed by the high-power electronics is wasted through the generation of heat. Such heat has to be rapidly dissipated; otherwise, the temperature of the electronics would increase, deteriorating their performance [1]. One option to address this dilemma is to encase the electronic devices in materials with sufficient thermal conductivity. Magnesium alloys seemed promising for this purpose because of their superior thermal conductivity compared to their plastic counterparts [2]. Meanwhile, the lightweight nature of Mg alloys brings about additional benefits associated with enhanced portability of electronic products [3].

Mg alloys are not readily available for housing electronics. The thermal conductivity of pure Mg is 156 W/(m·K), making it desirable for electronic appliances. However, the mechanical properties of pure Mg, with a tensile yield strength less than 150 MPa, are too low to provide essential mechanical protection to the electronic devices. Therefore, the demand for high-thermal-conductivity Mg alloys with robust mechanical performance is rapidly rising. The mechanical properties of pure Mg could be improved through alloying, which unfortunately, is usually accompanied by reduced thermal conductivity [4-6]. Consequently, finding ways to enhance the mechanical properties of Mg alloys while eliminating thermal conductivity degradation is a significant concern for both the academic and industrial communities.

It has been demonstrated that introducing crystalline defects, such as lattice distortions, in materials can influence both mechanical properties and thermal conductivity [7, 8]. Although lattice distortion typically has opposing effects to enhance mechanical properties while compromising thermal conductivity, it is feasible to strike a balance between the two aspects by selecting appropriate alloying elements. The elements possessing limited solubility in Mg lattice [9], similar atomic size [10], and identical valence numbers [11] to that of Mg, might introduce moderate lattice distortion, and

thus are desirable for maintaining its thermal conductivity. It has been reported that Al, Zn, Sn, Zr, Mn and Ca are all beneficial for improving the mechanical strength of pure Mg, albeit the resulting thermal conductivity is compromised in the following order Zn, Al, Ca, Sn, Mn [12]. Zn has appreciable solubility in Mg matrix and could induce profound lattice distortion, making it the most widely adopted element for strengthening Mg. Unfortunately, such strengthening effects are accompanied by the undesirable reduction in thermal conductivity. Introducing Zr into the binary Mg-Zn alloy significantly reduces the solid solubility of Zn in α-Mg by precipitating Zn_2Zr secondary phases, thus eliminating the lattice distortion to reduce thermal conductivity deterioration [13]. On the other hand, Zr is effective to refine the grain size to compensate for the reduced solid solution strengthening effect [14]. Ca is not expected to induce significant lattice distortion because of its notably low solubility, which makes it potential to develop Mg alloys with favorable thermal conductivity. Moreover, Ca could bring about additional benefits like microstructure refinement, texture weakening, and improved thermal stability to the Mg alloys [15]. Therefore, both the Mg-Zn-Zr [13] and Mg-Zn-Zr-Ca [16] alloys had been investigated to explore the possibility of simultaneously achieving high strength Mg alloys with good thermal conductivity and preliminary positive results have been reported. For instance, a balance between desirable thermal conductivity (130.0 W/(m·K)) and superior yield strength (227 MPa), as compared to pure Mg, has been achieved from a Mg-1.6Zn-0.4Zr-0.5Ca alloy [17]. Encouraged by the positive initial results, the balance between mechanical strength and thermal conductivity may be further fine-tuned through optimization of alloying element concentrations and thermomechanical processing parameters.

In this study, the Mg-4Zn-0.6Zr-xCa (x= 0, 0.3, 0.6, 0.9wt.%) alloy was formulated with the aim of attaining both high thermal conductivity and superior mechanical properties. Through an investigation of the alloy's microstructure, mechanical properties, and thermal conductivity, the impact of Ca content on dynamic recrystallization mechanisms, strengthening mechanisms, and thermal conductivity was analyzed. This research is anticipated to offer innovative insights for the development of metallic materials with elevated strength and thermal conductivity

suitable for heat sink structures.

2. Experimental details

2.1. Materials preparation

The materials with nominal composition of Mg-4Zn-0.6Zr-xCa (where x= 0, 0.3, 0.6, 0.9) were prepared using the conventional melting and casting method in this work. This process involved melting commercially pure magnesium, zinc granules, and master alloys Mg-25 wt.% Ca and Mg-30 wt.% Zr at a temperature of 973 K under the protection of a gas mixture containing SF_6 and CO_2. After refining, the melts were subjected to direct-chill casting to produce ingots with a diameter of 150 mm. The actual composition of the alloys was determined through inductively coupled plasma atomic emission spectroscopy (ICP-AES), and the results have been presented in **Table 1**. Following a 20-hour homogenization treatment at 653 K, the ingots were then machined to a final diameter of 130 mm to remove any surface defects and contaminants. Then the ingots were subjected to extrusion at 623 K with an extrusion ratio of 11, and a ram speed of 0.3 mm/s to get extrusion bars with diameter a of 38 mm.

Table 1 Actual chemical compositions of all designed alloys

Alloy Designation	Nominal Composition	Actual Composition by ICP (wt.%)			
		Mg	Zn	Zr	Ca
ZK41	Mg-4Zn-0.6Zr	*Bal.*	4.02	0.65	-
ZK413	Mg-4Zn-0.6Zr-0.3Ca	*Bal.*	3.90	0.58	0.27
ZK416	Mg-4Zn-0.6Zr-0.6Ca	*Bal.*	3.92	0.64	0.60
ZK419	Mg-4Zn-0.6Zr-0.9Ca	*Bal.*	3.99	0.56	0.96

2.2. Microstructure characterization

The microstructure of the as-extruded alloys was examined using an OLYMPUS BX51M metallographic optical microscope (OM) and a TESCAN/MIRA3 XMH scanning electron microscope (SEM). Prior to observation, specimens for both OM and SEM observation were meticulously polished to achieve a mirror-like surface free of any scratches using progressively refined sandpapers. Subsequently, the surface of the specimen was etched using a caustic solution consisting of 1 g oxalic acid, 1 ml acetic acid, 10 ml 10% nitrate alcohol, and 141 ml anhydrous ethanol. The average grain sizes

(AGS) of the as-extruded alloys were determined using the linear intercept method.

The phase compositions of the studied alloys were determined using a D/max 2550VB diffractometer, while their macro-textures were characterized using a D8 Advance X-ray diffractometer. Both the diffractometers were equipped with Cu Kα radiation (λ=0.1554 nm). For the purpose of phase identification, the diffractometer was operated in the Bragg-Brentano geometry with a 2θ range spanning from 20° to 80° with a step size of 0.02°and a scanning rate of 2 degrees per minute. The phase compositions of the samples were identified using a conventional search/match procedure, in accordance with the standard powder diffraction files incorporated in the MDI JADE 9.0 software.

Electron backscattered diffraction (EBSD) analysis was undertaken to study the DRX behavior of the samples using a JEOL JSM-7900F FEG-SEM with Oxford Instruments Symmetry EBSD. The EBSD data were acquired with a step size of 0.2 μm over an area of 240 μm × 180 μm. The EBSD specimen preparation involved mechanical grinding and polishing as reported in our previous work [18] . A Gatan precision etching and coating system (PECS) was employed for final polishing (5 keV beam and 4° angle for 15 minutes).

The distribution and crystallographic structure of the secondary phases were characterized using a Titan G2 60-300 transmission electron microscopy (TEM) operated with an accelerating voltage of 300 kV. The TEM specimens were prepared using a standard polishing and thinning procedure. Initially, the samples were cut, mechanically ground and punched to obtain discs with a diameter of 3 mm. Then the thickness of the discs was further reduced to approximately 50 μm. Perforation of the discs was achieved through twin-jet electropolishing, and finally, the thin region of the specimen was further expanded through ion beam thinning technique.

2.3. Tensile testing

The mechanical properties of the as-extruded samples were evaluated using the tensile tests following the ASTM E8M standard. The tensile samples possessed a gauge length of 25 mm, with a diameter of 5 mm in the reduced section. The tension tests were conducted at room temperature with a tension rate of 3.0×10^{-3} s^{-1} using a WANCE-

ETM1048 universal testing machine. Each sample had been tested for at least three times to ensure the reliability of the results.

2.4. Thermal diffusivity testing

The thermal diffusivity of the alloys was measured using a laser flash analyzer (TA Instrument DXF-500, USA) in both the transverse direction (TD) and extrusion direction (ED). The sample possessed a dimension of 12.7 mm × 3 mm. The room temperature density of the sample was determined using the water displacement method. Each test was conducted a minimum of three times to ensure repeatability.

The relationship between thermal conductivity and thermal diffusivity coefficient can be calculated using the following equation [19, 20]:

$$\lambda = \alpha \cdot \rho \cdot C_p \quad (1)$$

where λ is the thermal conductivity, α is the thermal diffusivity coefficient, ρ is the density and C_p is the specific heat capacity of alloys which can be expressed by the Neumann-Kopp law [20-22]:

$$C_P = \sum C_{Pi} x_i \quad (2)$$

Where C_{pi} and x_i, respectively, represents the specific heat capacity and mass fraction of the element i (i=Mg, Zn, Zr and Ca). The specific heat capacity of pure Mg, Zn, Zr and Ca at room temperature can be separately calculated using the following equations [23]:

$$C_P(Mg) = 0.890 + 4.58 \times 10^{-4} T \quad (3)$$

$$C_P(Zn) = 0.330 + 1.80 \times 10^{-4} T \quad (4)$$

$$C_P(Zr) = 0.257 + 0.10 \times 10^{-4} T \quad (5)$$

$$C_P(Ca) = 0.550 + 3.01 \times 10^{-4} T \quad (6)$$

where T is temperature.

3. Results and discussion

3.1. As-extruded microstructure

The optical microscopy images presented in Fig. 1 illustrated the microstructure of the as-extruded Mg-4Zn-0.6Zr-xCa alloys captured from the ED-TD plane. All the samples exhibited bimodal-grained microstructures, as characterized by the co-existence of the

large elongated grains (along ED) and the fine equiaxed grains. The alloy composition had a significant impact on the grain size distribution. With increasing Ca content, the large elongated grains became slimmer, and the fine grains decorating among them became more refined. The addition of Ca had a noticeable effect on the fraction of large elongated grains. Specifically, in the ZK41 alloy, approximately 30.9% of the observed surface was occupied by these grains. This value significantly decreased to 19.1% and 10.7% when 0.3 wt.% and 0.6 wt.% Ca was added, respectively. A slight increase in the fraction of elongated grains occurred with a further increase in Ca content to 0.9 wt.%. Such a bimodal grain size distribution is common in as-extruded Mg alloys [24, 25], and is attributed to the occurrences of incomplete DRX during hot working of the alloys. It is believed, and will be confirmed later by EBSD results, that the fine equiaxed grains resulted from the DRX process, while the large elongated grains were formed due to the deformation of the original grains. Consequently, it can be inferred that the addition of Ca promoted DRX during hot extrusion of Mg-Zn-Zr alloy.

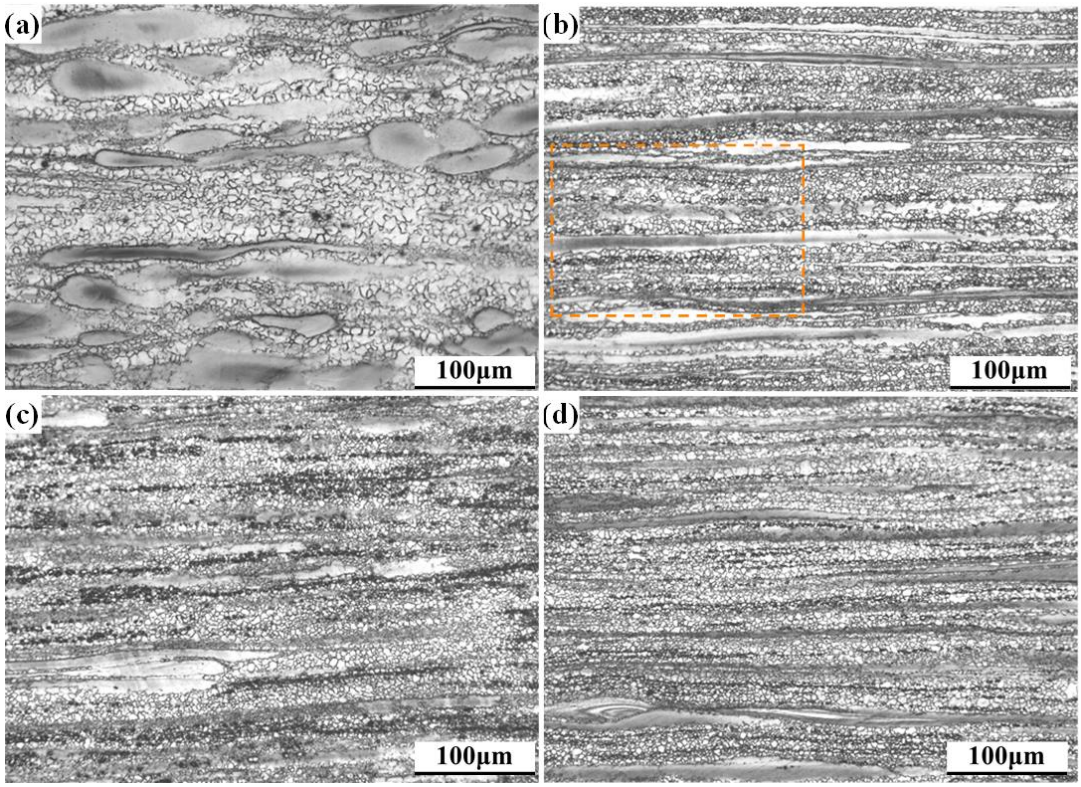

Fig. 1. The optical microscopy images of the as-extruded alloys viewed from the ED-TD plane (a) ZK41, (b) ZK413, (c) ZK416 and (d) ZK419 alloy

The optical microscopy images of the as-extruded Mg-4Zn-0.6Zr-xCa alloys captured from the plane normal to ED, are depicted in Fig. 2, confirming the bimodal grain size

distribution. The large grains, corresponding to the elongated grains observed in Fig. 1, exhibit an equiaxed appearance in Fig. 2. By combining the distinct characteristics shown in Fig. 1 and Fig. 2, it can be inferred that the large elongated grains resemble cylinders, with their axes aligned parallel to ED, and their dimensions along the axis are significantly greater than those in other directions. Additionally, it is evident that the fine grains exhibit equiaxed characteristics regardless of the observation direction.

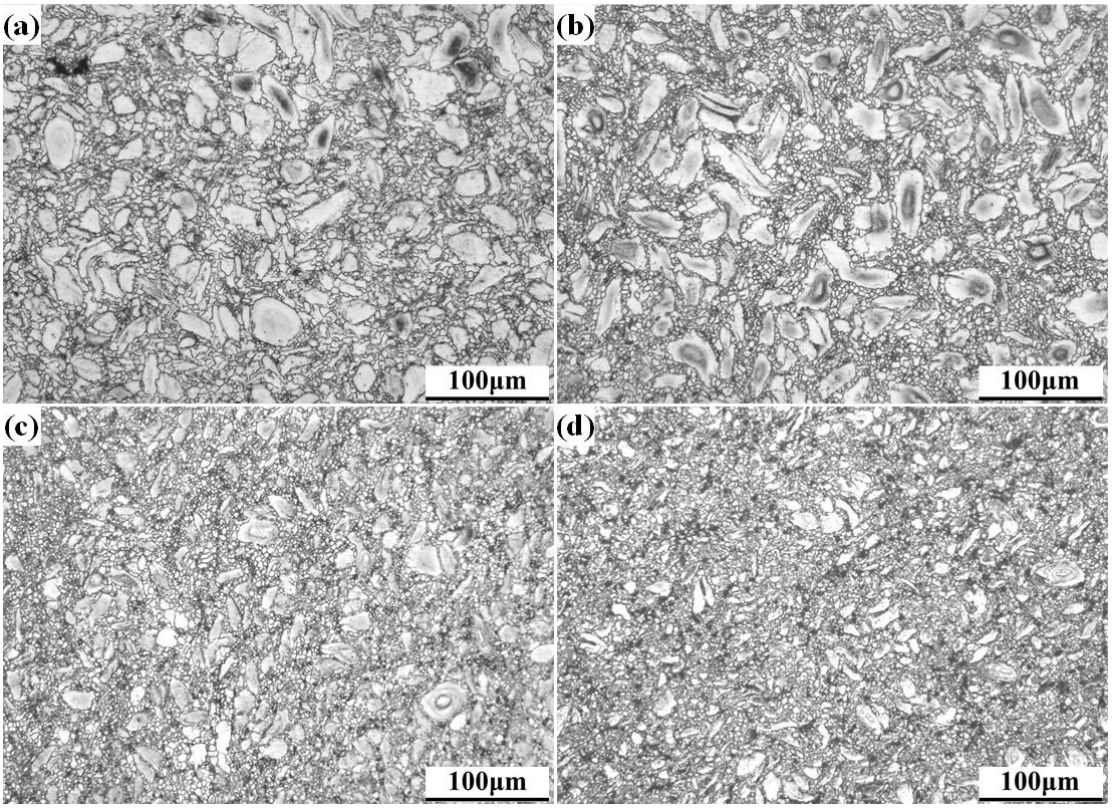

Fig. 2. The optical microscopy images of the as-extruded alloys viewed from the plane normal to ED (a) ZK41, (b) ZK413, (c) ZK416 and (d) ZK419 alloy

SEM images of the as-extruded alloys, acquired from the plane normal to ED, are depicted in Fig. 3. An appreciable number of secondary phases was observed in all the samples, and most of the fine secondary phases were distributed within the interior of the fine recrystallized grains, while coarser particles were also presented at the grain boundaries. These secondary phases primarily formed through the dynamic precipitation process during extrusion, as the pre-existing secondary phases had dissolved in the matrix during homogenization treatment before extrusion. The volume fraction of the secondary phases in the as-extruded ZK41, ZK413, ZK416, and ZK419 alloys were measured to be 1.26%, 2.92%, 5.56%, and 5.85%, respectively. Therefore,

Ca addition appears to facilitate the dynamic precipitation kinetics.

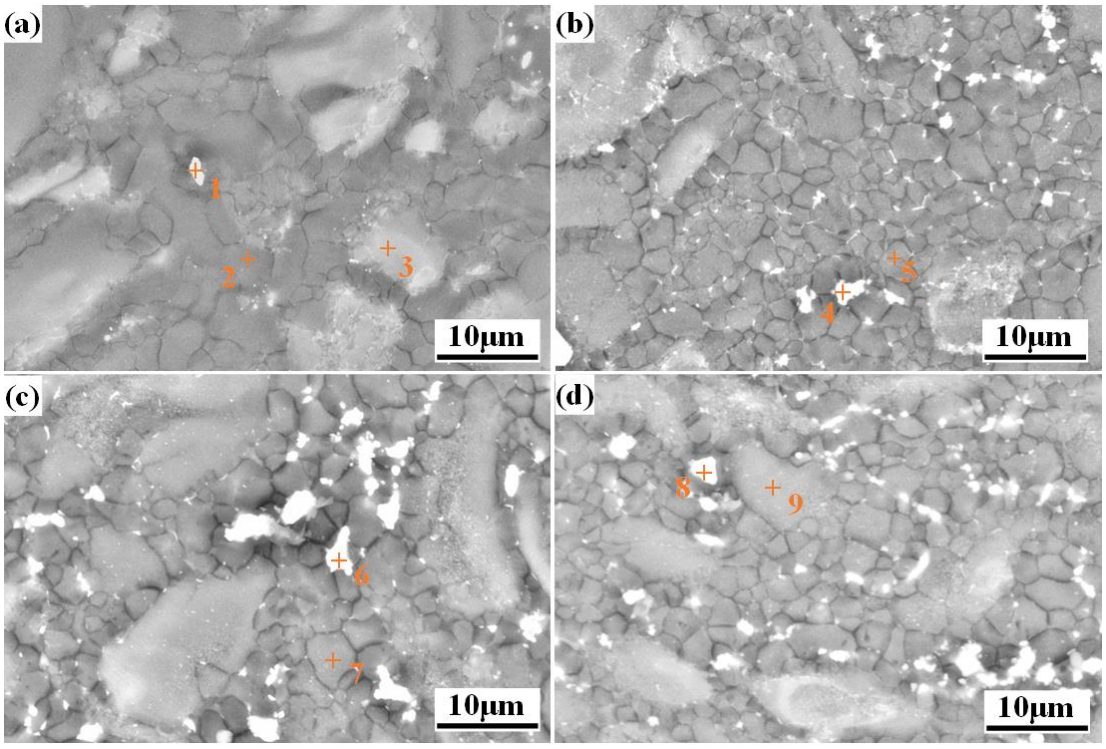

Fig. 3. The SEM images of the as-extruded captured from the plane normal to ED (a) ZK41, (b) ZK413, (c) ZK416 and (d) ZK419 alloy

The chemical compositions of various regions shown in Fig. 3 were characterized using the Energy Dispersive X-ray Spectroscopy technique, and the results are summarized in **Table 2**. It is clear that the secondary phases in the ZK41 alloy without Ca addition were enriched in Zr and Zn content (Region 1 in Fig. 3), while the α-Mg matrix (Region 2 in Fig. 3) had a chemical composition similar to the nominal composition of the alloy. After alloying with Ca, Ca was detected in both the α-Mg matrix and secondary phases. Specifically, the Ca content in the secondary phases (Region 4) of the ZK413 alloy was about 7 times that added to the alloy, while the α-Mg matrix (Region 5) contained almost identical Ca concentration to that shown in Table 1. When the sample was alloyed with 0.6 wt.% Ca, more Ca (~11.6 wt.%) was concentrated in the secondary phases, and the Ca concentration in the secondary phases (Region 8) remained almost unchanged even when the Ca content was further increased to 0.9 wt.% in the alloy.

Table 2 EDS results acquired from the various regions number in Fig. 3 (wt.%)

Elements	ZK41			ZK413		ZK416		ZK419	
	1	2	3	4	5	6	7	8	9
Mg	55.1	95.6	90.9	83.6	96.0	56.3	95.0	62.5	95.8
Zn	30.3	4.0	7.2	13.1	3.4	31.6	3.8	27.2	3.4
Zr	14.6	0.4	1.9	0.8	0.4	0.5	0.3	0.3	0.3
Ca	0	0	0	2.5	0.2	11.6	0.9	10.0	0.5

The EBSD inverse pole figure (IPF) maps of the as-extruded alloys under investigation have been collected and are depicted in Fig. 4. The bimodal grain size distribution, as observed in Fig. 1, was further confirmed by the IPF maps. However, the large and fine grains in the alloy exhibited distinct textures with respect to the sample orientation. The large elongated grains exhibited a preferential orientation, with their *c*-axis roughly perpendicular to ED. In contrast, the fine grains exhibit random orientation. Additionally, significant strains might have been stored in the large grains, as indicated by the color variation within them.

The grains were classified based on their Grain Orientation Spreads (GOS), following the commonly accepted practice in the literature. Specifically, grains with GOS $\leq 5°$ were categorized as dynamically recrystallized (DRXed) grains, while those with GOS greater than 5° were considered deformed grains [26]. It was evident that grains with GOS $\leq 5°$ aligned well with the fine, equiaxed grains, confirming that these fine grains were formed by the DRX process. In contrast, the large elongated grains exhibited apparent strain, resulting in a GOS higher than 5°. Consequently, these elongated grains were identified as deformed grains. It is important to note that some of the elongated grains with a GOS of $\leq 5°$ were also classified as deformed grains. During the hot extrusion process, dislocations typically multiply to accommodate plastic strains, resulting in a high GOS. However, dislocation annihilation through dynamic recovery and DRX can also occur, leading to a reduced GOS. Nevertheless, it is plausible that within certain grains, the locally stored energy is just sufficient to initiate dynamic recovery, without additional energy being available to complete DRX. In such cases, dislocations are annihilated (resulting in a reduced GOS), but the grains still maintain their deformed appearance. Utilizing this straightforward grain differentiation criteria

and in conjunction with the metallographic image presented in Fig. 1, the fraction of DRXed grains was calculated to be 69.1%, 80.9%, 89.3%, and 85.7% for the ZK41, ZK413, ZK416, and ZK419 alloys, respectively. The current results suggested that the Ca addition apparently improves the DRX extent in the alloy, as consistent with the existing literature [27, 28].

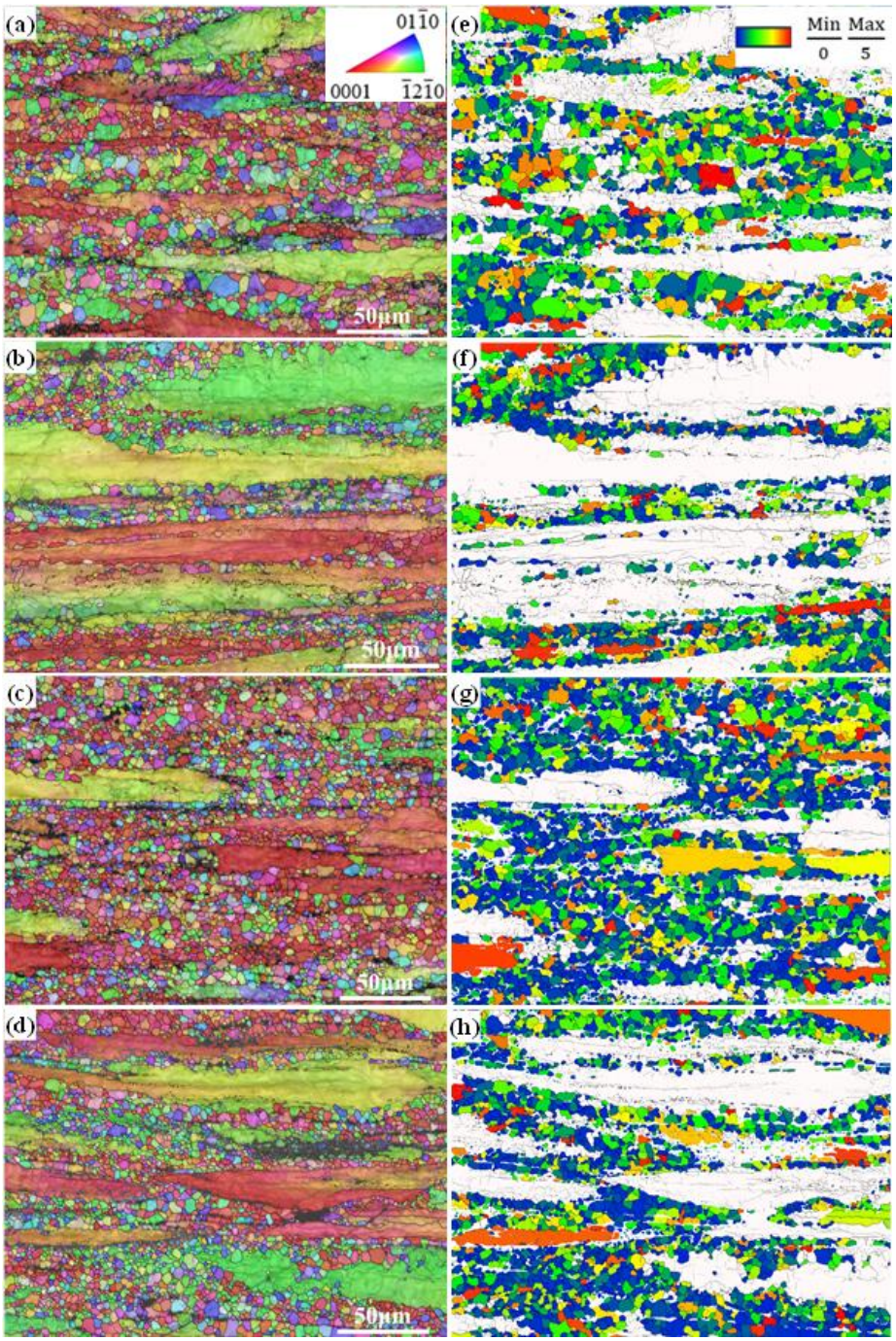

Fig. 4. EBSD IPF figure (a~d) and GOS maps (e~h) of the as-extruded alloys acquired from ED-TD plane (a,e) ZK41, (b,f) ZK413, (c,g) ZK416 and (d,h) ZK419.

Fig. 5 shows the (0001) pole figure and inverse pole figure of the extruded alloys. The

data presented in Fig. 5 were obtained through XRD measurements rather than EBSD analysis. The (0001) pole figures (Fig. 5(a-d)) indicated that all the samples possessed the typical extrusion texture [29], i.e., the majority of the grains aligned their basal plane paralleling to ED. Even though roughly identical (0001) polar intensity had been obtained among the samples, Ca content indeed induced different orientation characteristics. Specifically, an ideal extrusion texture would result in a uniform polar density (*c*-axes) distribution along TD within the range of 0-90°, which, however, was not observed in the present study. Instead, most grains had their *c*-axes, ununiformly, limited in a rather narrow range, 0-15°, along TD. More detailed orientation characteristics were revealed by the corresponding inverse pole figure shown in Fig. 5(e-h). In the ZK41 alloy, both the [11-20] and [10-10] basal fiber components were observed, with the [11-20] and [10-10] crystallographic directions parallel to ED (Fig. 5(e)), respectively. When the alloy was alloyed with Ca up to 0.3 wt.%, however, the [11-20] fiber component diminished, resulting in a basal texture with the [10-10] directions parallel to ED (Fig. 5(f, g)). Further increasing the Ca content to 0.9 wt.% changed the orientation characteristics, both the [11-20] and [10-10] fiber components could be equally observed (Fig. 5(h)).

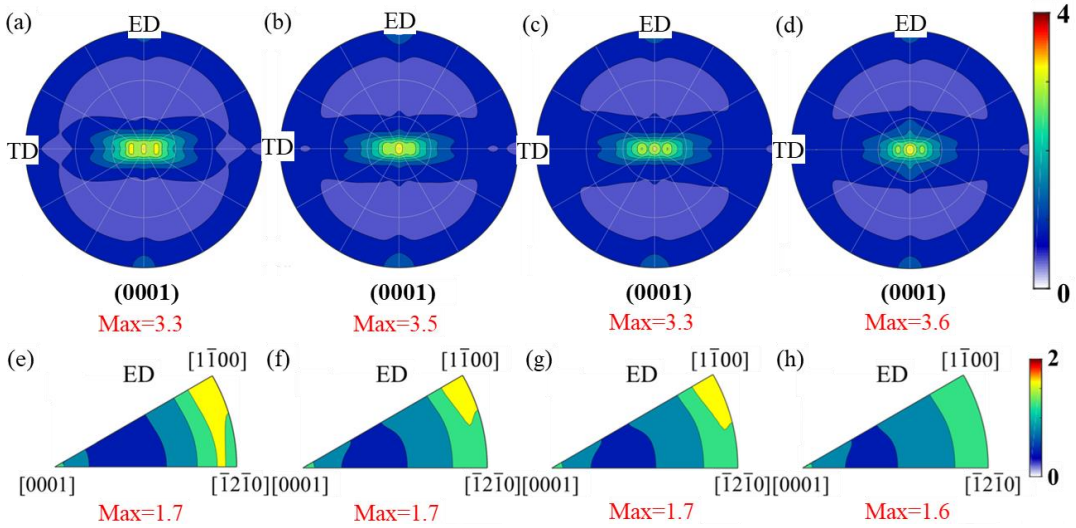

Fig. 5. (a-d) (0001) pole figures and (e-h) inverse pole figures of the studied alloys (a,e) ZK41, (b,f) ZK413, (c,g) ZK416 and (d,h) ZK419

Fig. 6 displays the Kernel Average Misorientation (KAM) maps for all the as-extruded

alloys, acquired from the ED-TD plane, aiming to quantify the spatial distribution of the lattice distortions. Generally, higher KAM values indicate higher misorientation or more pronounced lattice distortions [30]. The white regions presented in Fig. 6 are due to the insufficient indexing during EBSD data acquisition. It should be notified here that the EBSD images had been captured from a rather small area of 240 μm × 180 μm, which failed to represent the averaged microstructure characteristics of the studied alloys because of the apparent microstructure inhomogeneity (as proved in Fig.1). Therefore, the KAM values of the DRXed grains and the deformed grains were separately derived from Fig. 6. Then the KAM of the as-extruded samples were calculated based on the following equation (7):

$$KAM=V_{DRX}\cdot KAM_{DRX}+V_{def}\cdot KAM_{def} \quad (7)$$

where, V_{DRX} and KAM_{DRX} are, respectively, the volume fraction, and the averaged KAM values of the DRXed grains; V_{def} and KAM_{def} are, respectively, the volume fraction, and the averaged KAM values of the deformed (elongated) grains. The volume fraction of the DRXed and deformed grains were derived from the more representative optical metallographic image (shown in Fig 1) that had been captured from a larger area of 440 μm × 320 μm. Then the KAMs of the ZK41, ZK413, ZK416 and ZK419 alloys were determined to be 0.504°, 0.501°, 0.357° and 0.426°, respectively. It has been well-documented that KAM values are positively correlated with the lattice distortions[30], therefore, the addition of Ca in the ZK41 alloy may eliminate its lattice distortion, and the ZK416 alloy possessed the least lattice distortion among the studied alloys. During hot extrusion, the deformation of the alloys was accompanied with dislocation multiplication, which inevitably resulted in lattice distortion. On the other hand, the DRX process normally leads to dislocation annihilation [31]. Therefore, the large deformed grains typically exhibit a higher dislocation density compared to their DRXed counterparts. In this regard, the highest volume fraction of the DRXed grains in the ZK416 alloys rationalized its least KAM values.

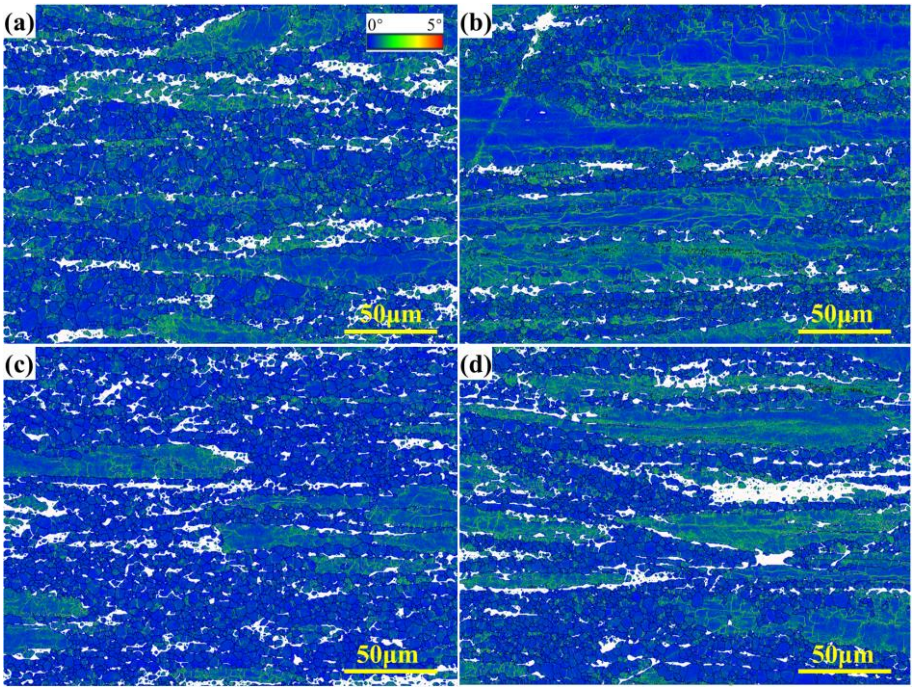

Fig. 6. (a)-(d) KAM maps after extrusion corresponding to (a) ZK41, (b) ZK413, (c) ZK416 and (d) ZK419 alloys with the observation direction perpendicular to ED.

The DRXed grains were extracted from the EBSD IPF map to analyze their grain size distribution, and the results were illustrated in Fig. 7. The DRX grains in the Ca-free ZK41 alloy had an average grain size of 4.7±2.6 μm, which apparently reduced after Ca addition. Specifically, the addition of 0.3 wt.% Ca into the alloy refined the DRX grains to 3.5±1.5 μm, and such value was slightly increased when the Ca content was further increased to 0.6 wt.% and 0.9 wt.% that yielded an average DRX grain size of 3.9±1.3 μm and 3.8±1.6 μm, respectively. It has been verified by the SEM image shown in Fig. 3 that Ca alloying enhanced secondary precipitation and refined the secondary phase particles. These precipitates would stimulate the DRX through the PSN (particle-stimulated nucleation) mechanism [32]. Therefore, the refined DRXed grains in the Ca-containing alloys can be attributed to their higher secondary phase particles fraction.

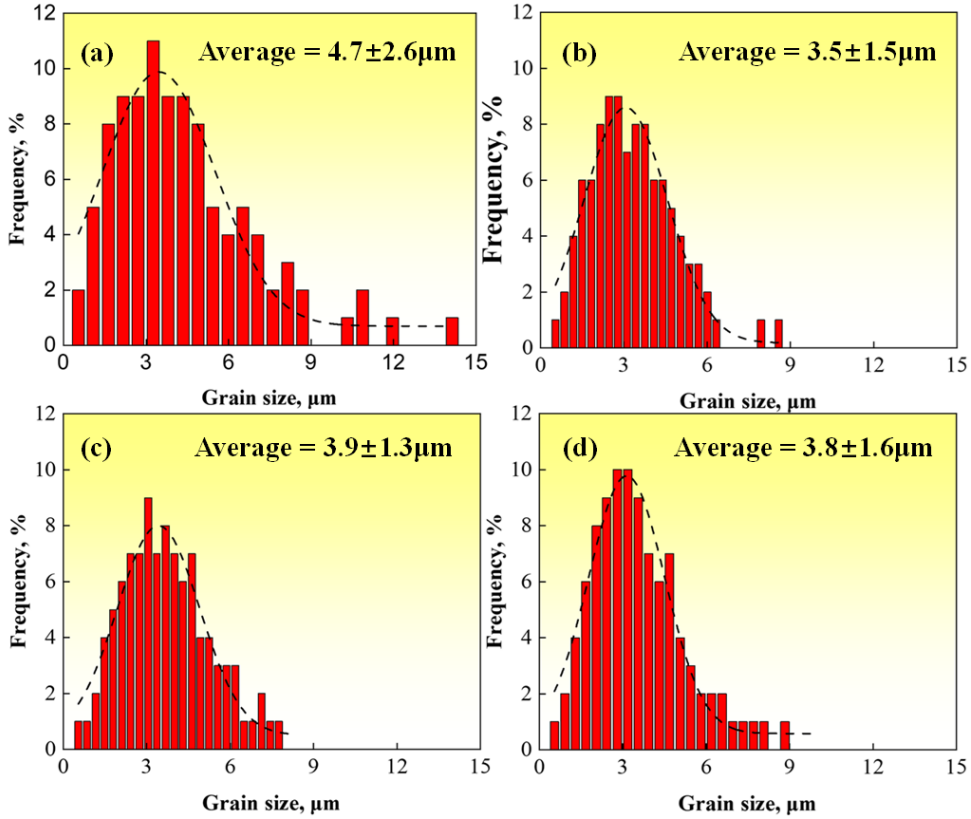

Fig. 7. Average DRXed grain size distribution of the as-extruded (a) ZK41, (b) ZK413, (c) ZK416 and (d) ZK419 alloys.

The phase compositions of the alloys under investigation were determined using the XRD technique, and the results are presented in Fig. 8. It is evident that all the alloys exhibited nearly identical diffraction patterns, irrespective of the Ca content. Mainly α-Mg were identified from the XRD characterization. No other secondary phase, other than a trace of $MgZn_2$ (as confirmed by the XRD peak at 2theta=44.0°), was observed in Fig. 3. Additionally, Ca alloying appeared to influence the XRD results by shifting the corresponding diffraction peaks. In Fig. 8(b), the diffraction peak associated with the (10-11) plane around 2theta = 36.6° are illustrated, along with their shift compared to the theoretical position. It is apparent that all the peaks shifted toward the lower 2theta direction, and the extent of the shift was influenced by the alloying compositions. Specifically, a shift of -0.36° was observed in the ZK41 alloy, while the addition of Ca led to shifts of -0.17°, -0.21°, and -0.13° for the ZK413, ZK416, and ZK419 alloys, respectively. The incorporation of alloying elements with different atomic sizes, the presence of secondary phases as well as the accumulated dislocations inevitably distorted the crystalline lattice, altering their interplanar spacings and contributing to

the shifting of the XRD peaks. However, it is difficult to determine which factor predominated, because the shifts observed in Fig 8 were the comprehensive results of the many influencing factors.

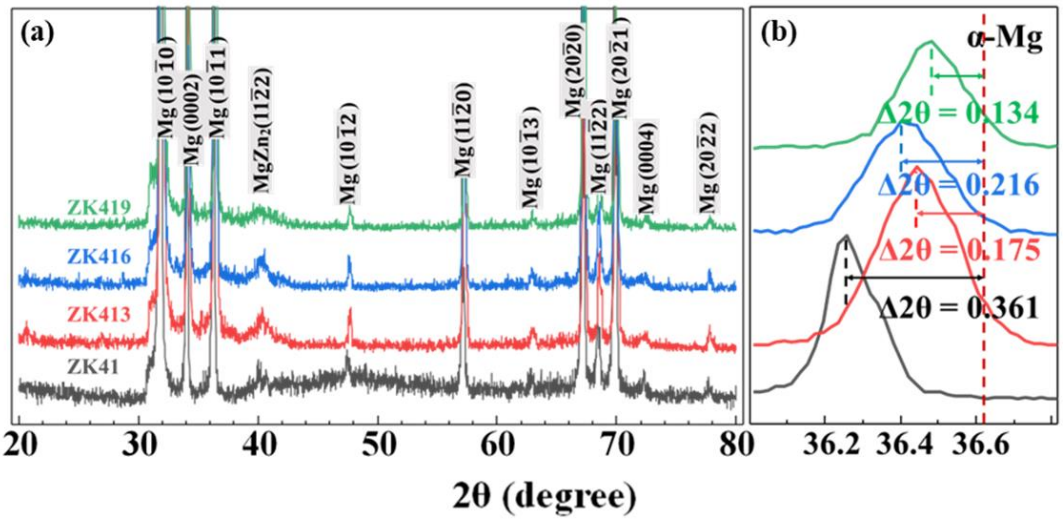

Fig. 8. (a)XRD patterns of the as-extrude Mg-4Zn-0.6Zr-xCa (x = 0, 0.3, 0.6, 0.9 wt.%) alloys and (b) The offset of the α-Mg peak near 2theta = 36.60 of the as-extrude Mg-4Zn-0.6Zr-xCa (x = 0, 0.3, 0.6, 0.9 wt.%) alloys.

TEM observations were conducted in the present study to characterize the crystalline structure of the secondary phases, as illustrated in Fig. 9. In the bright field image depicted in Fig. 9(a), two distinct regions labeled as B and C were identified. Selected area electron diffractions (SAED) were obtained from these regions, and the results are presented in Fig. 9(b~c). It is evident that region B constituted a ternary phase comprising Mg, Zn, and Ca (Fig. 9(d)), and the atomic ratio of Mg, Zn and Ca is close to 6:3:2. The SAED pattern in Fig. 9(b) indicated that this ternary phase possessed a hexagonal crystal structure and could be identified as $Ca_2Mg_6Zn_3$, in accordance with existing literature [33]. Furthermore, region C corresponded to the α-Mg matrix, as confirmed by its SAED pattern in Fig. 9(c).

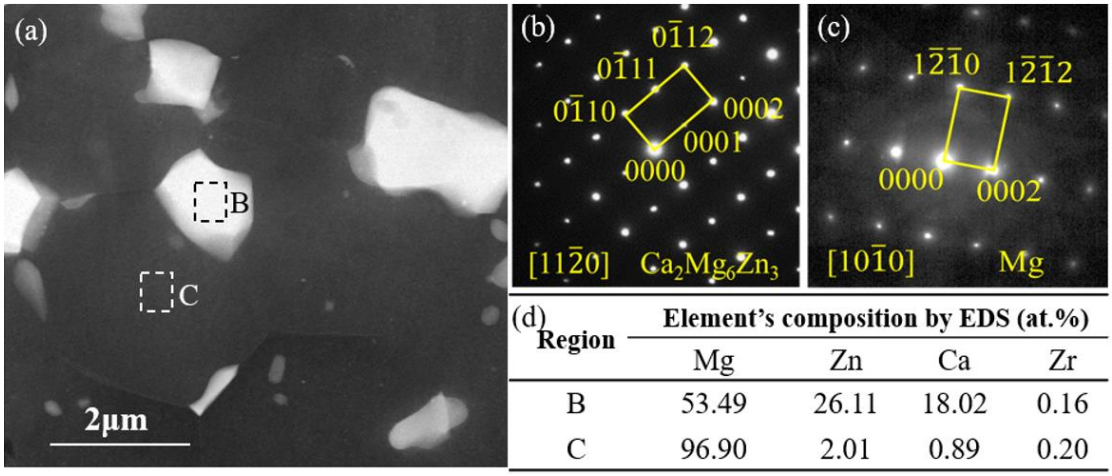

(d)

Region	Element's composition by EDS (at.%)			
	Mg	Zn	Ca	Zr
B	53.49	26.11	18.02	0.16
C	96.90	2.01	0.89	0.20

Fig. 9. (a) The HADDF-TEM image of the ZK416 alloy and (b, c) the corresponding SAED patterns of the distinct regions marked as B and C in (a), (d) the EDS chemical compositions of the distinct regions B and C in (a).

Fig. 10 provides a comparative representation of the bright field images for the Ca-free ZK41 alloy and the Ca-containing ZK416 alloy. These two alloys exhibited distinct characteristics. In the ZK41 alloy (Fig. 10(a)), several secondary phases with a diameter less than 0.2 μm were evident within the grain interior and along the grain boundaries. Additionally, both DRXed grains and deformed grains were observable. The DRXed grains exhibited a typical hexagonal shape with an average size of around 2 μm, characterized by the absence of discernible dislocations. Conversely, traces of dislocations are noticeable in the deformed grains, as indicated in Fig. 10(a), and smaller DRXed grains are also present along the boundaries of the deformed grains.

In contrast, the scenario in the ZK416 alloy differs significantly. Besides the minute secondary phases within the grain interior, much larger secondary phases of approximately 2 μm were situated at the grain boundary triple junctions. No deformed grains were identified in the observed region (Fig. 10(b)). It is worth mentioning that the High Angle Annular Dark Field-Scanning Transmission Electron Microscope (HAADF-TEM) images indicated that both ZK41 and ZK416 have a large amount of nanoscale precipitated phase in the grain after extrusion deformation, there are also some $Ca_2Mg_6Zn_3$ phases with a diameter of about 100 nm in ZK416 alloy.

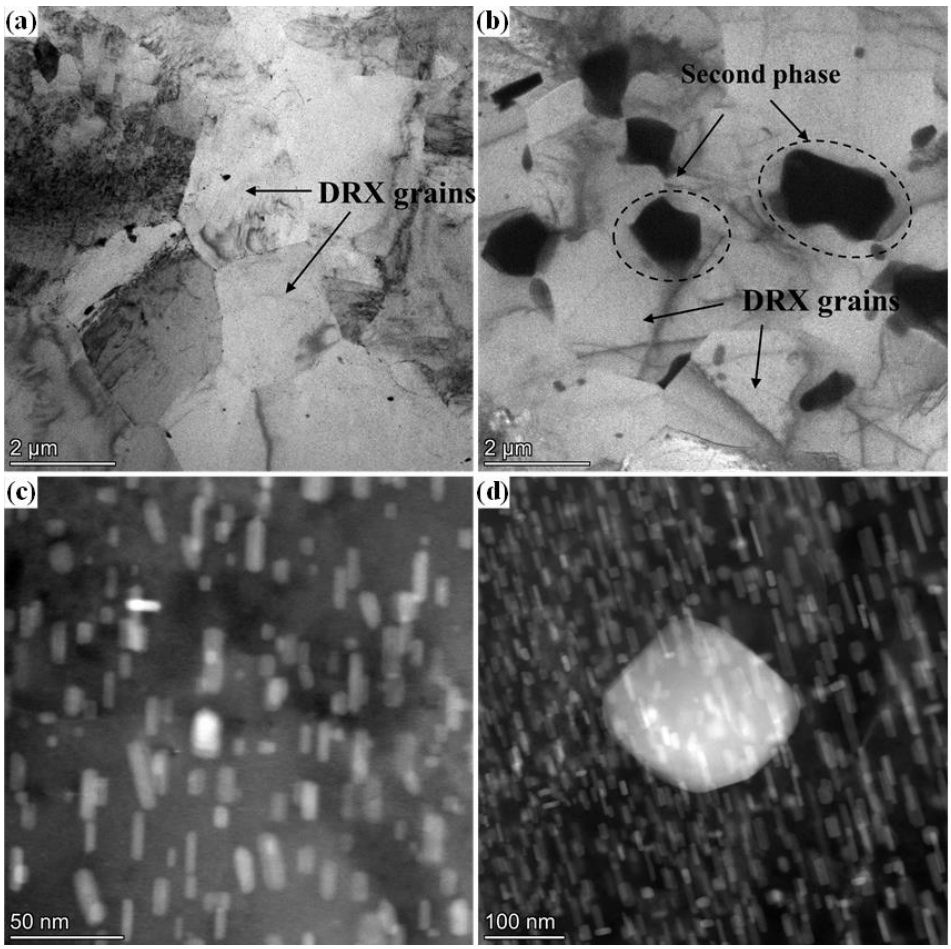

Fig. 10. Bright Field and HAADF-STEM images
(a,c) ZK41 and (b,d) ZK416 alloy.

3.2. Mechanical properties

Fig. 11 illustrates the engineering stress-strain curves for all as-extruded alloys, providing insight into the impact of Ca additions on the mechanical properties of the Mg–4Zn-0.6Zr alloy. As depicted, the addition of Ca clearly strengthened the alloy at the expense of the fracture elongation (FE). The point at which the curve deviated from a linear behavior was taken as the yielding point. For the ZK41 alloy, the yield strength (YS), ultimate tensile strength (UTS), and FE are 234 MPa, 307 MPa, and 23.7%, respectively. The addition of 0.3 wt.% Ca increased the YTS by 12.8% to 273 MPa, which further rose to 298 MPa with an increase in Ca content to 0.9 wt.%. Concurrently, the elongation of the ZK41 alloy decreased to 15.5% after adding 0.9 wt.% Ca.

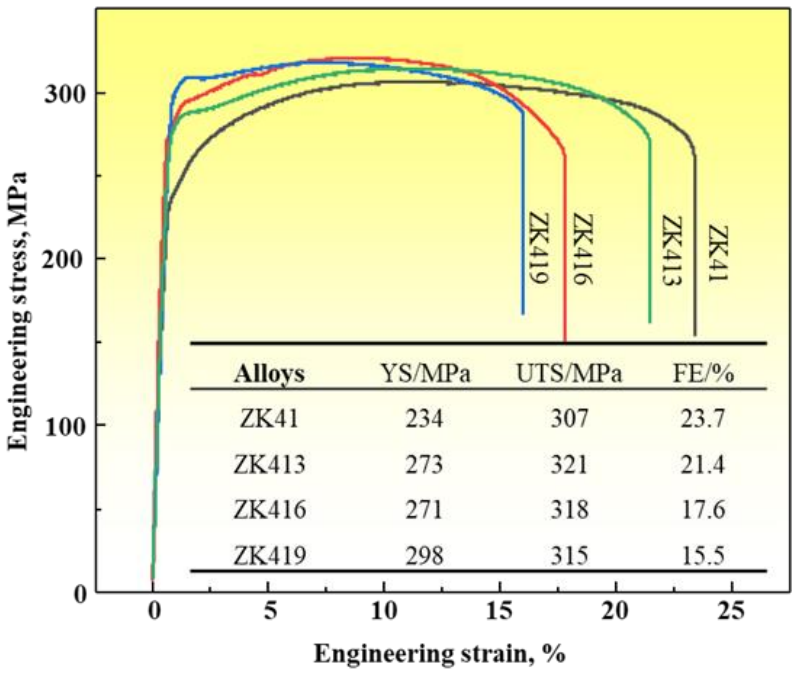

389

390 Fig. 11. The tensile curve and mechanical properties of the studied as-extruded alloys.

391 The enhanced mechanical strength of the Mg-Zn-Zr alloy with the addition of Ca can
392 be attributed to both microstructure refinement and densely distributed precipitates. It
393 has been verified in Fig. 1 that the addition of Ca remarkably refined the microstructure
394 of the alloys, which may lead to an increase in the yield strength according to the well-
395 known Hall-Petch relationship [34]. On the other hand, Ca alloys apparently promotes
396 the dynamic precipitation process during hot extrusion, resulting in more densely
397 distributed secondary phase particles with reduced sizes in the grain interior and also
398 along the grain boundaries of the Ca-containing alloy as compared with the Ca-free
399 ZK41 alloy. The precipitates at grain boundaries may impose anchoring effect on the
400 grain boundary sliding, contributing to the increased YTS. The precipitates in the grain
401 interior may impede the dislocation movements through the Orowan mechanism,
402 increasing the YTS of the alloy [35].

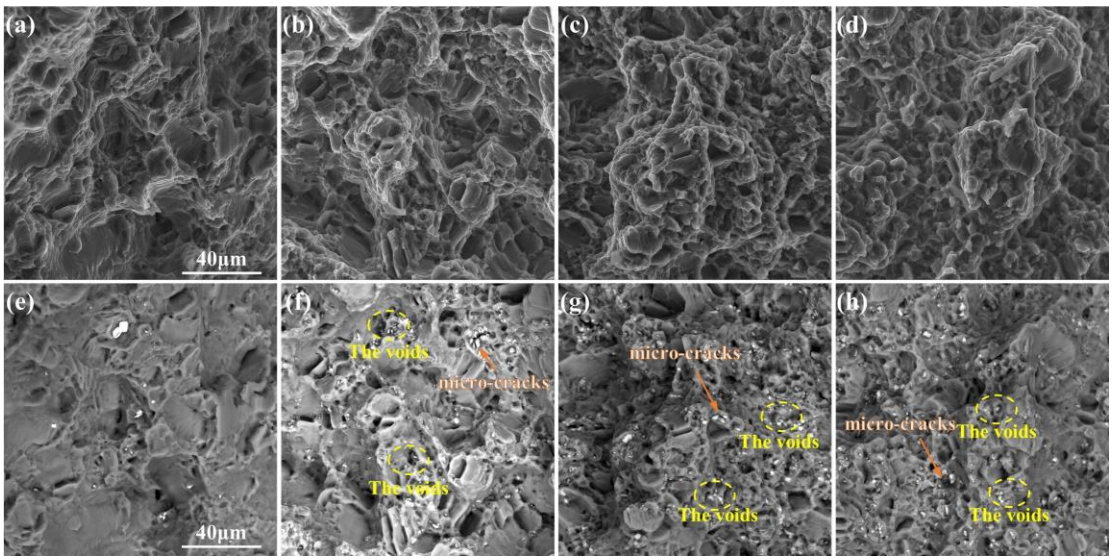

Fig. 12 SEM images of fracture morphology after tensile tests corresponding to (a) (e) ZK41, (b) (f) ZK413, (c) (g) ZK416 and (d) (h) ZK419 alloys.

The tensile fracture topography of all the alloys is presented in Fig. 12. It is evident that ductile fracture occurred in all the alloys, as indicated by the presence of numerous dimples. Throughout the tensile test, substantial plastic deformation occurred in the alloy. At the interface between the matrix and the secondary phases, deformation incompatibility occurred, leading to the nucleation of voids. Actually, plenty of micro cracks can be observed at the vicinity of the secondary phase particles, as marked in Fig. 12. The nucleation, growth, and coalescence of these voids ultimately resulted in the formation of dimples in the fracture surface [36]. This well-established ductile fracture mechanism underscores the significance of secondary phases in dimple formation. In the present study, the addition of Ca increased the volume fraction and refined the average size of the secondary phases (Fig. 3), facilitating the void nucleation during the tensile test. Furthermore, the presence of secondary phases at the grain boundaries amplified stress magnitudes, leading to the formation of micro-cracks and, ultimately, premature fracture of the alloys. Therefore, the reduced elongation observed in the Ca-containing alloys can be primarily attributed to the increased number of secondary phase particles in the alloy.

3.3. Thermal conductivity

The thermal diffusivity of the as-extruded alloys was measured, and the corresponding

thermal conductivity was calculated using Equation (1). The results, presented in **Table 3**, highlighted a significant influence of Ca content on the thermal conductivity of the as-extruded alloys. The Ca-free ZK41 alloy exhibited a thermal conductivity of approximately 113.3 W/(m·K) along ED. The addition of Ca substantially increased the thermal conductivity to around 118 W/(m·K) for all Ca-containing alloys.

Furthermore, the thermal conductivity displayed some anisotropy depending on the testing direction. Notably, all samples measured along TD exhibited considerably higher thermal conductivity than those measured along ED, possibly due to the apparent texture characteristics of the alloys [29]. The ZK416 alloy possessed the highest thermal conductivity of 128.9 W/(m·K) along TD.

It had been reported that HCP metals normally have higher thermal conductivity along the *c*-axis other than along the *a*-axis [37]. As the majority of the grains in the studied alloys tend to align their basal planes parallel to ED (Fig. 5), the thermal conductivity measured along ED approximately arise from the *a*-axis while that measured in TD roughly correlated with the *c*-axis thermal conductivity. In the present study, the average of the thermal conductivity, λ_{ave}, measured from both the TD and ED was taken as the nominal thermal conductivity of the studied alloys.

Table 3 Experimental parameters for thermal conductivity (λ) calculation.

Alloys	α_{ED} mm²/s	α_{TD} mm²/s	ρ g/cm³	C_p J/(g·K)	λ_{ED} W/(m·K)	λ_{TD} W/(m·K)	λ_{ave} W/(m·K)
ZK41	62.85±1.09	68.70±0.33	1.81	0.996	113.3±1.9	123.8±0.6	118.6±1.3
ZK413	64.92±1.53	70.41±1.22	1.82	0.995	117.7±2.7	127.6±2.2	122.6±2.5
ZK416	64.75±1.00	70.18±0.16	1.85	0.994	118.9±1.8	128.9±0.3	123.9±1.1
ZK419	64.49±1.37	68.28±1.13	1.83	0.993	117.2±2.4	124.1±2.0	120.1±2.2

There are many factors affecting the thermal conductivity of magnesium alloys, including solute atoms, secondary phases and the internal strains [38]. Any factor that can intensify the lattice distortion may compromise the thermal conductivity of the alloys by enhancing phonon scattering and reducing the mean free path of the valence electrons. Solute atoms and internal strains inevitably cause lattice distortion to reduce

447 the thermal conductivity of alloys, while the secondary phases precipitation is normally
448 considered beneficial in enhancing the thermal conductivity by consuming the solutes
449 to relieve the lattice distortion [39].

450 In the present study, the α-Mg lattice accommodates roughly the same number of solute
451 atoms (**Table 2**), which may not induce the profound thermal conductivity variations
452 observed among the samples. Further, the lattice distortion caused by the residual
453 strains as confirmed by the KAM (Fig. 6) and XRD analysis (Fig. 8) may have
454 contributed to the thermal conductivity variation. Based on the XRD results shown in
455 Fig. 8, the lattice parameters of the alloys were calculated and presented in **Table 4**.
456 The deviation of lattice volume from that of pure Mg was taken to describe the extent
457 of lattice distortion [39, 40]:

458 $$|\Delta| = V - V_0 \quad (8)$$

459 All the alloys exhibited significant lattice distortion compared to perfect Mg crystals,
460 with the distortion decreasing in the following order: ZK41 > ZK413 > ZK419 > ZK416.
461 ZK41 and ZK416 alloys, respectively, demonstrate the maximum and minimum lattice
462 distortion, which resulted in the minimum and maximum thermal conductivity as
463 outlined in **Table 3**.

464 **Table 4 Lattice parameter and volumes of Mg Solution in the studied alloys.**

Alloys	Lattice parameters			
	$a(Å)$	$c(Å)$	$V(Å^3)$	$\Delta(Å^3)$
Pure Mg	3.209	5.210	46.46	-
ZK41	3.234	5.240	47.46	1.00
ZK413	3.217	5.222	46.79	0.33
ZK416	3.211	5.209	46.51	0.05
ZK419	3.211	5.216	46.57	0.11

465 The current study reveals that the addition of Ca simultaneously enhances the
466 mechanical strength and thermal conductivity of the ZK41 alloy. Fig. 13 compares the
467 thermal conductivity and yield strength obtained in the present study with that
468 published in the literature [38, 41-46], it is clear that the ZK416 alloy in the present
469 study, possessing a YTS of 271 MPa and a thermal conductivity of 123.9 W/(m·K)
470 outperforms most of the reported results. The combination of high yielding strength and

superior thermal conductivity makes the ZK416 alloy potentially more suitable for practical application, such as in electronic areas, where high strength and good thermal conductivity are of primary concern.

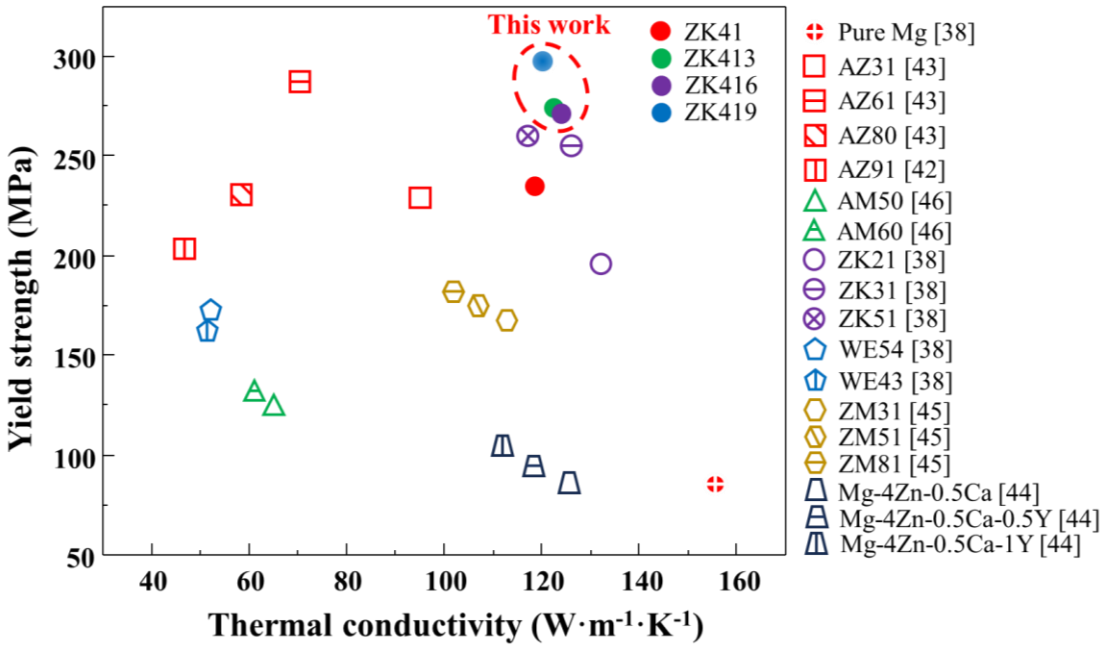

Fig. 13. Thermal conductivity versus yield strength of some reported alloys and alloys in this work.

4. Conclusion

In this work, Mg-4Zn-0.6Zr-*x*Ca (*x*= 0, 0.3, 0.6 and 0.9wt%) alloys with varying Ca content were prepared through extrusion. The effects of Ca content on the microstructures, mechanical properties and thermal conductivities of the alloys were evaluated. Ca elements not only refined the microstructure by facilitating dynamic recrystallization but also promoted the dynamic precipitation of secondary phases, thus improving the mechanical properties of the alloys. Both the DRX and precipitation process eliminated the lattice distortion of α-Mg, leading to an exceptional thermal conductivity. An extraordinary combination of mechanical strength (YTS of 271 MPa) and thermal conductivity (123.9 W/(m·K) was achieved when 0.6 wt.% Ca was added to the alloy. The current results provide insights on developing high strength Mg with superior thermal conductivity for electronic applications.

Data availability statement

The raw and processed data required to support the findings will be made available

from the authors upon reasonable request.

Originality statement

The authors confirm that the article has not been submitted to peer review, nor has been accepted for publishing in another journal. The authors also confirm that the research in this work is original, and that all the data given in the article are real and authentic. If necessary, the article can be recalled, and errors corrected.

Acknowledgements

The work was financially supported by the Postgraduate Innovative Project of Central South University (Grant No. 2022XQLH044). DG and XZ appreciates the support from the UKRI MRC Future Leaders Fellowship (Grant No. MR/T019123/2) and Royal Society International Exchanges 2021 Cost Share (NSFC) (Grant No. IEC\NSFC\211323). The discussion on the macro texture of the alloys with Prof. Jianguo Tang was greatly appreciated.

References

[1] C. Tan, Z. Dong, Y. Li, H. Zhao, X. Huang, Z. Zhou, J.-W. Jiang, Y.-Z. Long, P. Jiang, T.-Y. Zhang, A high performance wearable strain sensor with advanced thermal management for motion monitoring, Nature communications 11(1) (2020) 3530.
[2] L. Chen, S. Lü, W. Guo, J. Li, S. Wu, High thermal conductivity of highly alloyed Mg-Zn-Cu alloy and its mechanism, J Alloy Compd 918 (2022) 165614.
[3] J. Rong, J.-N. Zhu, W. Xiao, X. Zhao, C. Ma, A high pressure die cast magnesium alloy with superior thermal conductivity and high strength, Intermetallics 139 (2021) 107350.
[4] Y. Liu, X. Qiao, Z. Li, Z. Xia, M. Zheng, Effect of nano-precipitation on thermal conductivity and mechanical properties of Mg-2Mn-xLa alloys during hot extrusion, Journal of Alloys and Compounds 830 (2020) 154570.
[5] V. Bazhenov, A. Koltygin, M. Sung, S. Park, Y.V. Tselovalnik, A. Stepashkin, A. Rizhsky, M. Belov, V. Belov, K. Malyutin, Development of Mg–Zn–Y–Zr casting magnesium alloy with high thermal conductivity, Journal of Magnesium and Alloys 9(5) (2021) 1567-1577.
[6] M. Yamasaki, Y. Kawamura, Thermal diffusivity and thermal conductivity of Mg–Zn–rare earth element alloys with long-period stacking ordered phase, Scripta Materialia 60(4) (2009) 264-267.
[7] M. Zhao, W. Pan, Effect of lattice defects on thermal conductivity of Ti-doped, Y2O3-stabilized ZrO2, Acta materialia 61(14) (2013) 5496-5503.
[8] A. Alghamdi, T. Maconachie, D. Downing, M. Brandt, M. Qian, M. Leary, Effect of additive manufactured lattice defects on mechanical properties: an automated method for the enhancement of lattice geometry, The International Journal of Advanced Manufacturing Technology 108 (2020) 957-971.
[9] Y. Zhang, Z. Zhang, H. Kang, H. Nagaumi, X. Yang, Development of an extremely dilute Mg-Mn-Ce alloy with high strength-thermal conductivity synergy by low-temperature extrusion, Materials Letters 326 (2022) 132965.
[10] P. Klemens, R. Williams, Thermal conductivity of metals and alloys, International metals reviews 31(1) (1986) 197-215.

[11] A. Schindler, E. Salkovitz, Brillouin zone investigation of Mg Alloys. I. Hall effect and conductivity, Physical Review 91(6) (1953) 1320.
[12] H. Pan, F. Pan, R. Yang, J. Peng, C. Zhao, J. She, Z. Gao, A. Tang, Thermal and electrical conductivity of binary magnesium alloys, Journal of Materials Science 49 (2014) 3107-3124.
[13] B. Li, L. Hou, R. Wu, J. Zhang, X. Li, M. Zhang, A. Dong, B. Sun, Microstructure and thermal conductivity of Mg-2Zn-Zr alloy, Journal of Alloys and Compounds 722 (2017) 772-777.
[14] M. Sun, D. Yang, Y. Zhang, L. Mao, X. Li, S. Pang, Recent advances in the grain refinement effects of Zr on Mg alloys: a review, Metals 12(8) (2022) 1388.
[15] Y. Zhang, L. Song, X. Chen, Y. Lu, X. Li, Effect of Zn and Ca addition on microstructure and strength at room temperature of as-cast and as-extruded Mg-Sn alloys, Materials 11(9) (2018) 1490.
[16] R. Zheng, T. Bhattacharjee, S. Gao, W. Gong, A. Shibata, T. Sasaki, K. Hono, N. Tsuji, Change of deformation mechanisms leading to high strength and large ductility in Mg-Zn-Zr-Ca alloy with fully recrystallized ultrafine grained microstructures, Scientific Reports 9(1) (2019) 11702.
[17] R. Zheng, T. Bhattacharjee, A. Shibata, T. Sasaki, K. Hono, M. Joshi, N. Tsuji, Simultaneously enhanced strength and ductility of Mg-Zn-Zr-Ca alloy with fully recrystallized ultrafine grained structures, Scripta Materialia 131 (2017) 1-5.
[18] D. Guan, W.M. Rainforth, L. Ma, B. Wynne, J. Gao, Twin recrystallization mechanisms and exceptional contribution to texture evolution during annealing in a magnesium alloy, Acta Materialia 126 (2017) 132-144.
[19] L. Zhong, Y. Wang, H. Luo, C. Luo, J. Peng, Evolution of the microstructure, texture and thermal conductivity of as-extruded ZM60 magnesium alloy in pre-compression, J Alloy Compd 775 (2019) 707-713.
[20] Y. Liu, X. Jia, X. Qiao, S. Xu, M. Zheng, Effect of La content on microstructure, thermal conductivity and mechanical properties of Mg–4Al magnesium alloys, Journal of Alloys and Compounds 806 (2019) 71-78.
[21] J. Leitner, P. Voňka, D. Sedmidubský, P. Svoboda, Application of Neumann–Kopp rule for the estimation of heat capacity of mixed oxides, Thermochimica Acta 497(1-2) (2010) 7-13.
[22] A. Rudajevová, F. Von Buch, B. Mordike, Thermal diffusivity and thermal conductivity of MgSc alloys, Journal of Alloys and Compounds 292(1-2) (1999) 27-30.
[23] K.C. Mills, Recommended values of thermophysical properties for selected commercial alloys, Woodhead Publishing2002.
[24] M. Zha, S.-Q. Wang, T. Wang, H.-L. Jia, Y.-K. Li, Z.-M. Hua, K. Guan, C. Wang, H.-Y. Wang, Developing high-strength and ductile Mg-Gd-Y-Zn-Zr alloy sheet via bimodal grain structure coupling with heterogeneously-distributed precipitates, Materials Research Letters 11(9) (2023) 772-780.
[25] L. Fan, M. Zhou, W. Lao, Y. Zhang, H. Dieringa, Y. Zeng, Y. Huang, G. Quan, Improving the ductility and toughness of nano-TiC/AZ61 composite by optimizing bimodal grain microstructure via extrusion speed, Journal of Magnesium and Alloys (2023).
[26] A. Hadadzadeh, F. Mokdad, M. Wells, D. Chen, A new grain orientation spread approach to analyze the dynamic recrystallization behavior of a cast-homogenized Mg-Zn-Zr alloy using electron backscattered diffraction, Materials Science and Engineering: A 709 (2018) 285-289.
[27] M. Hradilová, F. Montheillet, A. Fraczkiewicz, C. Desrayaud, P. Lejček, Effect of Ca-addition on dynamic recrystallization of Mg–Zn alloy during hot deformation, Materials Science and Engineering: A 580 (2013) 217-226.
[28] M. Nienaber, J. Bohlen, S. Yi, G. Kurz, K.U. Kainer, D. Letzig, Influence of Ca addition on the dynamic and static recrystallization behavior of direct extruded flat profiles of Mg-Y-Zn alloy, Journal of Magnesium and Alloys 11(10) (2023) 3736-3748.
[29] Y. Zhang, T. Chen, J. Kuang, Q. Huo, Relationship Between Work Hardening Capacity and Compressive Creep Behavior in a Hot-Extruded Mg–6Al–1Zn Alloy Rod, Metallurgical and Materials Transactions A 53(3) (2022) 747-753.
[30] S.-S. Rui, Q.-N. Han, X. Wang, S. Li, X. Ma, Y. Su, Z. Cai, D. Du, H.-J. Shi,

Correlations between two EBSD-based metrics Kernel Average Misorientation and Image Quality on indicating dislocations of near-failure low alloy steels induced by tensile and cyclic deformations, Materials Today Communications 27 (2021) 102445.
[31] F. Dalla Torre, R. Lapovok, J. Sandlin, P.F. Thomson, C.H.J. Davies, E.V. Pereloma, Microstructures and properties of copper processed by equal channel angular extrusion for 1–16 passes, Acta materialia 52(16) (2004) 4819-4832.
[32] K. Huang, K. Marthinsen, Q. Zhao, R.E. Logé, The double-edge effect of second-phase particles on the recrystallization behaviour and associated mechanical properties of metallic materials, Progress in Materials Science 92 (2018) 284-359.
[33] R. Schäublin, M. Becker, M. Cihova, S.S. Gerstl, D. Deiana, C. Hébert, S. Pogatscher, P.J. Uggowitzer, J.F. Löffler, Precipitation in lean Mg–Zn–Ca alloys, Acta Materialia 239 (2022) 118223.
[34] J.-w. Kang, C.-j. Wang, K.-k. Deng, K.-b. Nie, Y. Bai, W.-j. Li, Microstructure and mechanical properties of Mg-4Zn-0.5 Ca alloy fabricated by the combination of forging, homogenization and extrusion process, Journal of Alloys and Compounds 720 (2017) 196-206.
[35] B. Du, Z. Xiao, Y. Qiao, L. Zheng, B. Yu, D. Xu, L. Sheng, Optimization of microstructure and mechanical property of a Mg-Zn-Y-Nd alloy by extrusion process, Journal of Alloys and Compounds 775 (2019) 990-1001.
[36] H.G. Wilsdorf, Void initiation, growth, and coalescence in ductile fracture of metals, Journal of Electronic Materials 4 (1975) 791-809.
[37] J. Yuan, K. Zhang, T. Li, X. Li, Y. Li, M. Ma, P. Luo, G. Luo, Y. Hao, Anisotropy of thermal conductivity and mechanical properties in Mg–5Zn–1Mn alloy, Materials & Design 40 (2012) 257-261.
[38] S. Li, X. Yang, J. Hou, W. Du, A review on thermal conductivity of magnesium and its alloys, Journal of Magnesium and Alloys 8(1) (2020) 78-90.
[39] J. Rong, W. Xiao, Y. Fu, X. Zhao, P. Yan, C. Ma, M. Chen, C. Huang, A high performance Mg–Al–Ca alloy processed by high pressure die casting: Microstructure, mechanical properties and thermal conductivity, Materials Science and Engineering: A 849 (2022) 143500.
[40] Z. Li, B. Hu, D. Li, W. Zhang, X. Zeng, Z. Lin, C. Jin, S. Zhao, Microstructure-dependent thermal conductivity and mechanical properties in cast Mg-4Sm-xAl alloys, Materials Science and Engineering: A 861 (2022) 144336.
[41] M.M. Avedesian, H. Baker, ASM specialty handbook: magnesium and magnesium alloys, ASM international Materials Park, OH1999.
[42] Q. Chen, Z. Zhao, D. Shu, Z. Zhao, Microstructure and mechanical properties of AZ91D magnesium alloy prepared by compound extrusion, Materials Science and Engineering: A 528(10-11) (2011) 3930-3934.
[43] S. Mueller, K. Mueller, H. Tao, W. Reimers, Microstructure and mechanical properties of the extruded Mg-alloys AZ31, AZ61, AZ80, International journal of materials research 97(10) (2006) 1384-1391.
[44] G.-Y. Oh, Y.-G. Jung, W. Yang, S.K. Kim, H.K. Lim, Y.-J. Kim, Investigation of thermal conductivity and mechanical properties of Mg-4Zn-0.5 Ca-xY alloys, MATERIALS TRANSACTIONS 56(11) (2015) 1887-1892.
[45] J. Yuan, High Thermal Conductivity Mg-Zn-Mn Alloy and its Properties, B, Res. Inst. Nonferr. Metal (2013).
[46] A. Rudajevová, M. Staněk, P. Lukáč, Determination of thermal diffusivity and thermal conductivity of Mg–Al alloys, Materials Science and Engineering: A 341(1-2) (2003) 152-157.